

# Extraction of Dielectric Permittivity from Atomistic Molecular Dynamics Simulations and Microwave Measurements

Published as part of *The Journal of Physical Chemistry* virtual special issue "Jose Onuchic Festschrift".

Alex Saad-Falcon, Zijian Zhang, David Ryoo, James Dee, Ryan S. Westafer, and James C. Gumbart\*



Cite This: *J. Phys. Chem. B* 2022, 126, 8021–8029



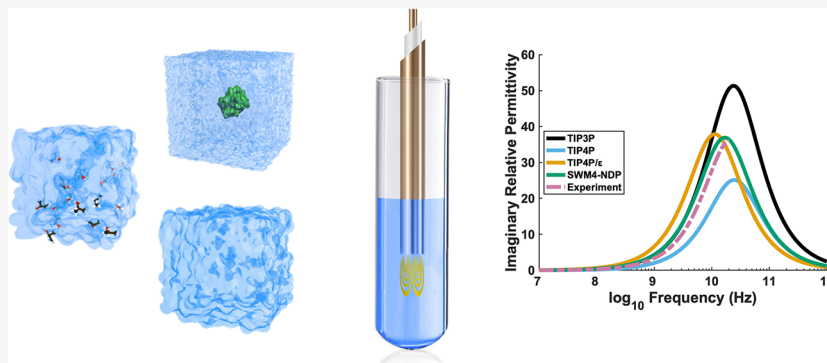
Read Online

ACCESS |

Metrics & More

Article Recommendations

Supporting Information



**ABSTRACT:** The design of new biotechnology depends on the prediction and measurement of the electrical properties of biomolecules. The dielectric permittivity, in particular, is highly important for the design of microwave systems for diagnostics, yet this property is rarely explicitly targeted during the development of biomolecular force fields for molecular dynamics (MD) simulations. In order to explore the ability of existing force fields to reproduce the frequency-dependent permittivity, we carried out MD simulations of various aqueous solutions, including pure water, isopropyl alcohol, alanine, and the protein ubiquitin. The TIP3P, TIP4P, TIP4P/ $\epsilon$ , and SWM4-NDP water models were used along with the CHARMM36m and Drude protein force fields. An experimental setup using a truncated coaxial line was created to measure the permittivity of the same solutions to check for measurement-model agreement. We found that one of the nonpolarizable force fields (TIP4P/ $\epsilon$  + CHARMM36m) and the polarizable force fields (SWM4-NDP + Drude) closely agree with experimental results. This demonstrates the strength of the tuned TIP4P/ $\epsilon$  water model, as well as the physical validity of polarizable force fields in capturing dielectric permittivity. This represents an important step toward the predictive design of biosensors.

## INTRODUCTION

Computer modeling and simulations have become indispensable tools in the design of modern technologies.<sup>1</sup> This is also becoming increasingly true at the molecular scale for bionanotechnology,<sup>2</sup> examples of which include DNA and protein sequencing by nanopores,<sup>3,4</sup> nanoparticle-based delivery systems,<sup>5</sup> and sensors made from DNA origami.<sup>6,7</sup> Obtaining quantitative results from these simulations requires accurate modeling of both the biological and abiotic components as well as their interface(s), in addition to the water in which they typically operate.

It is often the case that a bionanotechnological device will interface with an electrical circuit, putting particular emphasis on the ability of computational models to capture the dielectric permittivity, i.e., the degree to which a material polarizes in response to an applied electric field, of the device components.<sup>8</sup> Methods for calculating the permittivity from the dynamics of the underlying molecules in an aqueous

solution have been developed<sup>9–13</sup> and applied to simulations<sup>14–17</sup> over several decades. Additionally, various techniques have been designed to experimentally measure the permittivity of solutions.<sup>18–20</sup>

In this paper, we use molecular dynamics to simulate pure water as well as aqueous solutions of isopropyl alcohol (IPA), alanine, and ubiquitin using different nonpolarizable (TIP3P,<sup>21</sup> TIP4P,<sup>21</sup> TIP4P/ $\epsilon$ ,<sup>22</sup> CHARMM36m<sup>23</sup>) and polarizable (SWM4-NDP,<sup>24</sup> Drude-2013<sup>25</sup>) force fields. From the resulting trajectories, we compute the time auto/cross-correlation functions of the dipole moment for the solvent

Received: July 25, 2022

Revised: September 17, 2022

Published: September 28, 2022



and solute and derive the dielectric permittivity from them. Experimentally, we perform serial dilutions of each of the solutes and measure the complex reflection coefficient ( $S_{11}$ ) of the solutions with respect to an open-ended coaxial probe. We then use a calibration method<sup>18</sup> to compute the dielectric permittivity ( $\epsilon_r$ ) from the measured  $S_{11}$ . Comparisons between our measurements and simulations show measure-model fit, and our values for the permittivities match the literature closely. We find that the permittivity-adjusted TIP4P/ $\epsilon$  and SWM4-NDP water models align best with our measurements. The nonpolarizable TIP4P/ $\epsilon$  model requires less computational resources than the polarizable SWM4-NDP. However, the polarizable model better represents the underlying phenomena behind dielectric permittivity, which produces accurate results without fine-tuning.

## METHODS

**Simulation System Generation.** The water boxes were generated using the Solvate plugin in VMD. Following a previous study, we have adopted a (32 Å)<sup>3</sup> water box, which contains 995 water molecules, as a standard.<sup>26</sup> The other pure water systems had dimensions of the standard multiplied by one-half, two, three, or four.

The IPA systems were generated by placing IPA molecules within a standard water box and removing water molecules until the desired concentration was reached without changing the overall volume. Concentrations of 715.3, 357.6, 178.8, and 89.4 mg/mL were tested.

Solvated alanine systems were generated using the Molefactory plugin in VMD. To reflect different alanine concentrations in the standard (32 Å)<sup>3</sup> water box, we have placed 9, 15, and 21 alanine molecules to represent 50, 100, and 150 mg/mL respectively. Before solvating the system, the alanines were placed to be at least 5 Å apart from each other initially.

The ubiquitin systems were generated by using the crystal structure (PDB ID: 1UBQ).<sup>27</sup> The water box size was calculated according to the concentrations used previously.<sup>28</sup> Specifically, for the 1.14 mmol/dm<sup>3</sup> (~10 mg/mL) system, the dimensions of the water box used for a single copy of ubiquitin were (113 Å)<sup>3</sup>, and for the 2.28 mmol/dm<sup>3</sup> (~20 mg/mL) system, the dimensions were (90 Å)<sup>3</sup>.

**Molecular Dynamics.** All molecular dynamics simulations were performed using NAMD.<sup>29,30</sup> The force fields used for simulation of water are TIP3P,<sup>21</sup> TIP4P,<sup>21</sup> TIP4P/ $\epsilon$ ,<sup>22</sup> and SWM4-NDP,<sup>24</sup> while for proteins, the CHARMM36m<sup>23</sup> or Drude-2013 force field<sup>25,31,32</sup> was used. The TIP3P water model is composed of three particles: two hydrogen atoms and one oxygen atom. TIP4P and TIP4P/ $\epsilon$  models have an extra Lennard-Jones site (via a lone pair particle) attached to the oxygen atom along the molecule's bisector, which improves the electrostatic potential around the water molecule. TIP4P/ $\epsilon$  is a modestly tuned version of TIP4P with the objective of more accurately reproducing the dielectric permittivity of pure water. SWM4-NDP is a 5-site water model. Besides three atoms and a Lennard-Jones site, this model also contains an auxiliary particle attached to the oxygen atom via a zero-length harmonic spring to reproduce induced electronic polarization.

All simulations were performed using periodic boundary conditions with a cutoff at 12 Å for short-range electrostatics and Lennard-Jones interactions and a switching function starting at 10 Å. The particle-mesh Ewald method<sup>33</sup> with a grid spacing of ~1 Å was used for long-range electrostatic

interaction calculations. These long-range interactions are critical for correctly modeling the bulk dielectric properties of the system. Other techniques for modeling electrostatics include hierarchical methods<sup>34</sup> or the use of a reaction field.<sup>35</sup> Bonds between a heavy atom and a hydrogen atom were maintained to be rigid, while all other bonds remained flexible. All systems using a nonpolarizable force field were simulated at 300 K and 1 bar with a time step of 2 fs; those using polarizable SWM4-NDP and Drude-2013 force fields used a 1 fs time step. Each system was equilibrated for 10 ns in an isothermal-isobaric ensemble (NPT) first. Then, it was equilibrated for at least 40 ns in a canonical ensemble (NVT). A Langevin thermostat with a damping coefficient of 1 ps<sup>-1</sup> was used for temperature control, and a Langevin piston with a period of 0.3 ps and decay of 0.15 ps was used for pressure control. VMD was used for all visualization.<sup>36</sup>

Simulations of pure water were run for 100 ns. For IPA, alanine, and ubiquitin systems, each simulation was run for 250 ns with two replicas. The total simulation time was around 17 μs. In the frequency domain, the simulation times for the pure water and solutions lead to a lowest measurable frequency of 10 and 4 MHz, respectively.

**Molecular Dynamics Permittivity Extraction.** Once the simulations of the different solutions are completed, the permittivity must be extracted from the trajectories. Atomistic molecular dynamics simulations inherently calculate the electrostatic interactions of each atom with every other atom in the simulation. As such, the response of the overall system to an electrically large electromagnetic (EM) wave may be calculated based on the individual atomic trajectories. The response function of a system to an EM wave is based on the evolution of its dipole moment with respect to some waveform, so the first step of this procedure is to calculate the dipole moment of a subset of atoms in the system as

$$\vec{M}_i(t) = \sum_{n \in i} q_n(t) \vec{x}_n(t) \quad (1)$$

where  $q_n(t)$  and  $\vec{x}_n(t)$  are the partial charge and position of atom  $n$  in the  $i$ th subsystem of interest in the simulation at time  $t$ .<sup>37</sup> From there, the time series of dipole moments of each subsystem are correlated to determine how the evolution of one system impacts another or itself. These correlation functions take the form

$$\Phi_{i,j}(t) = \langle \vec{M}_i(\tau) \cdot \vec{M}_j(t + \tau) \rangle_\tau = \frac{1}{T} \sum_{\tau=0}^{T-t} \vec{M}_i(\tau) \cdot \vec{M}_j(t + \tau) \quad (2)$$

where the correlations are averaged for multiple starting times ( $\tau$ ) up to the total length of the simulation ( $T$ ) to improve the statistical validity for the estimate of correlation at time delay  $t$ . While methods exist to estimate the autocorrelation of dipole moments using shorter time series data, these methods typically build upon more complex models of the signal of interest.<sup>17</sup> As a result, this effort solely focused on lengthening simulations to achieve convergence of the autocorrelation. For a more in-depth study of these models, the reader is referred to Berne et al.<sup>38</sup> As a basic verification of simulation accuracy, the static permittivity may be calculated based on the time averages of the statistical moments of the electrical dipole moment.<sup>9,10,14</sup> For the extraction of frequency-dependent behavior, it becomes necessary to estimate the relation of the system's state at each time step to all subsequent states.<sup>11–13</sup>

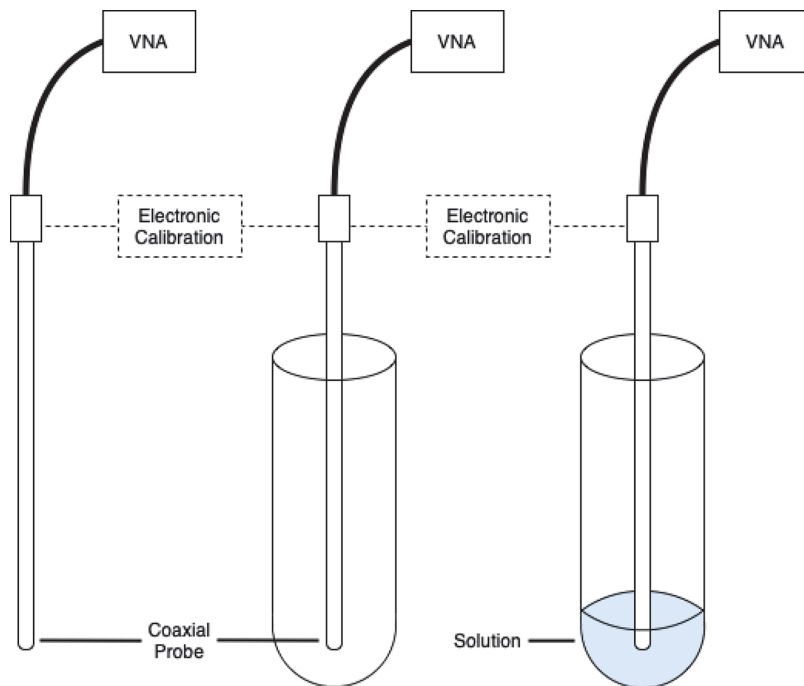


**Figure 1.** Measurement setup for open, empty, and water measurements. The VNA electronic calibration reference plane is indicated, at the connector to the semirigid coaxial probe.

By calculating the above autocorrelation function, the system is reduced to a model in which some smooth system response is hidden among noisy data points.<sup>15</sup> The electric susceptibilities ( $\chi$ ) of the individual subsystems may then be summed to determine the complex permittivity of the simulated system. The explicit form of this process is written as

$$\epsilon(\omega) = 1 + \sum_{i,j} \chi_{i,j}(\omega) = 1 + \frac{1}{3kVT} \sum_{i,j} \mathcal{L}[-\dot{\Phi}_{i,j}(t)] \quad (3)$$

where  $\mathcal{L}$  denotes the Laplace transform, and the dot notation indicates the time derivative of the auto/cross-correlation function.<sup>16</sup> One major technical step for the present effort was the development of a means to estimate the best-fit exponential for a given correlation function. This was achieved by approximating the time series of the correlation function as a set of Debye relaxations, where a Levenberg–Marquardt (LM) algorithm was used to converge to a stable best estimate of the time-series dynamics.<sup>39,40</sup> The complex-valued electric susceptibility and permittivity were then calculated as the analytic equivalents of this time-series best-fit. Further refinement of these calculations may also be implemented to account for highly conductive solutions in the future.<sup>41–43</sup> Likewise, for simulation geometries with nonzero total charge, the average net dipole moment can be subtracted from the dipole moment at each step to better estimate changes to the correlations between time steps.<sup>44</sup>

For each relaxation mechanism in a system, fields above the relaxation frequency oscillate faster than the underlying mechanism, and so the permittivity contribution of that resonance decreases to zero. Thus, it is expected that in the high-frequency limit, the susceptibility of the entire system will decrease to zero, making the permittivity unity. While this should be captured correctly by polarizable models due to their ability to capture at least some changes in the electron distribution, for nonpolarizable models, the only relaxation

mechanisms are those for which molecular reorientation occurs, limiting the accuracy of their high-frequency response. However, the fitting procedure developed here effectively enforces the correct high-frequency limit, which is why the permittivity for even nonpolarizable models approaches unity at high frequencies here. Details of the extension to satisfy the high-frequency limit can be found in Caillol et al.<sup>42,43</sup>

**Microwave Measurements and Permittivity Computation.** To perform microwave permittivity measurements, we created an open-ended coaxial probe by shearing and smoothing a coaxial line. The probe was verified under a microscope to have sufficiently smooth features. Following this, the probe was connected to a Keysight E8363C vector network analyzer (VNA). The network analyzer was electronically calibrated to the connector for the coaxial probe as shown in Figure 1.

First, we performed several measurements with the coaxial probe in the air. Measurements were taken in various probe orientations to verify repeatability. A measurement was also taken with the tip of the coaxial probe pressed against a metal surface to create a short circuit. Next, the probe was suspended above the test tube location using a measurement apparatus. Several measurements were taken both in the absence of a test tube and with an empty test tube for comparison. Finally, the coaxial probe was used to measure the complex reflection coefficient from solutions of deionized water and serial dilutions of IPA, alanine, and ubiquitin. The measurement setup is shown in Figure 1. For each solution, 500  $\mu$ L of liquid was used, and the measurement apparatus ensured uniform probe depth in the test tube. Ten frequency sweeps were performed from 10 MHz to 20 GHz, and no significant inconsistencies were seen across the ten sweeps.

Each measurement produced a complex reflection coefficient ( $S_{11}$ ) at frequencies ranging from 10 MHz to 20 GHz. Because the SMA connector to the coaxial probe was not perfectly matched, the return loss ( $20 \log_{10}|S_{11}|$ ) over frequency

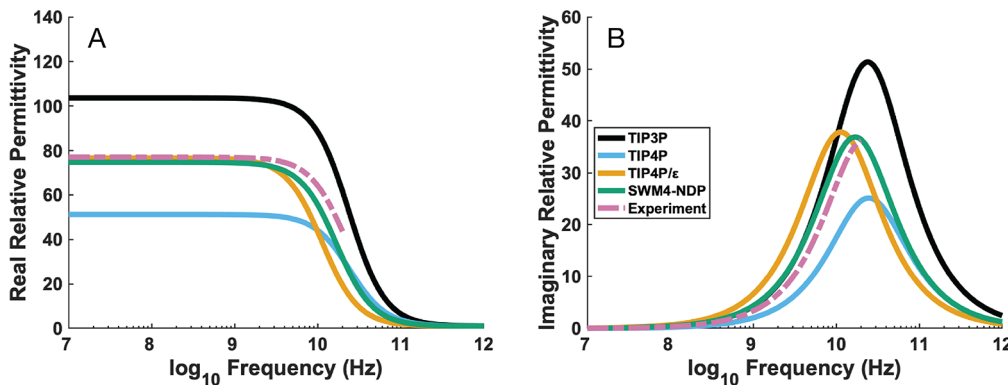


**Figure 2.** Verification of extraction of complex permittivity for four different water models: TIP3P, TIP4P, TIP4P/ε, and SWM4-NDP. (A) Real and (B) imaginary parts of the complex frequency-dependent permittivities. The domain is from 10 MHz to 1 THz. See Figure S2 for replicas of the TIP3P and TIP4P/e water models.

contained oscillations that correspond to resonance peaks and nulls along the length of the coaxial probe. The inverse Fourier-transformed return loss also showed echoes of the main return at integer multiples of the propagation time along the probe. To address these oscillations/echoes, time gating was applied to the resulting  $S_{11}$  time data, and this was verified to eliminate the oscillation artifacts after Fourier transform back to the frequency domain. The return loss before and after time gating is shown in Figure S1.

We then used the PyOECP library<sup>45</sup> to extract the dielectric permittivity from the  $S_{11}$  measurements for each of our solutions. This library implements the antenna calibration method proposed by Marsland and Evans,<sup>18</sup> which requires four calibration measurements of known loads. The first measurement is typically taken to be a short circuit. For the other three standards, we used our open circuit, water, and 715.3 mg/mL IPA measurements. The experimental permittivities for alanine and ubiquitin use this calibration method. The reference permittivity for water is that of Kaatze,<sup>19</sup> and the reference permittivity of IPA is from Sato et al.<sup>20</sup> We also tested the calibration method with other references for water and IPA,<sup>46,47</sup> but these did not result in any significant difference in permittivity. Solutions were agitated sufficiently to ensure there was no detectable aggregation. We also note that no precipitates were observed in the solutions before or after the measurements.

## RESULTS

**Pure Water Permittivity.** Before extracting the permittivity of solutions from simulations, we first computed the permittivity of the solvent: water. The simulated permittivities of different water models, namely TIP3P, TIP4P, TIP4P/ε, and SWM4-NDP, were compared to experiments in Figure 2. These simulations were run for 100 ns using a (32 Å)<sup>3</sup> water box. We found that the water permittivity converges after 40 ns (Figure S3). Larger systems also produce the same permittivity (Figure S4), which indicates that the water box size used is sufficient.

The real permittivities of the TIP4P/ε and SWM4-NDP models are near 75 in the low frequency regime. This value is slightly lower than the canonical water permittivity of ~78 from experiments at 300 K.<sup>19</sup> The TIP4P/ε and SWM4-NDP models perform much better than TIP3P and TIP4P, whose permittivities are above 100 and below 60, respectively. These results are similar qualitatively to van der Spoel et al.,<sup>35</sup> where

it was shown that using a reaction field also results in TIP3P overestimating and TIP4P underestimating the dielectric constant of pure water.

For the imaginary portion of pure-water permittivity, the resonance magnitudes of TIP3P and TIP4P are much higher and lower, respectively, than the value from experiments. The TIP4P/ε water model represents the imaginary permittivity peak properly in magnitude, but the location of the peak is at a slightly lower frequency than the canonical resonance (Figure 2 and Tables 1 and 2).

**Table 1. Peak Frequency of Imaginary System Permittivity (GHz)**

system	TIP3P	TIP4P/ε	Drude	exptl
water only	24.0	11.4	16.9	21.6
isopropyl alcohol 89.4 mg/mL	18.6	8.3	11.2	7.5
isopropyl alcohol 178.8 mg/mL	14.5	5.9	7.7	4.7
isopropyl alcohol 357.6 mg/mL	8.6	3.6	3.9	1.9
isopropyl alcohol 715.3 mg/mL	2.0	1.3	1.0	0.5
alanine 50 mg/mL	19.6	9.3	12.5	19.1
alanine 100 mg/mL	14.6	7.4	9.6	19.0
alanine 150 mg/mL	11.9	4.6	0.7	18.7
ubiquitin 10 mg/mL	23.4	10.9	15.7	19.9
ubiquitin 20 mg/mL	22.5	10.7	15.6	20.0

The polarizable SWM4-NDP water model represents the resonance frequency and magnitude properly and performs best among all tested models. Unlike the other three water models tested, SWM4-NDP has a unique Drude particle,

**Table 2. Peak Magnitude of Imaginary System Permittivity ( $\epsilon''_r$ )**

system	TIP3P	TIP4P/ε	Drude	exptl
water only	51.3	37.9	36.9	36.3
isopropyl alcohol 89.4 mg/mL	45.1	34.5	34.0	26.7
isopropyl alcohol 178.8 mg/mL	38.5	30.4	30.3	18.8
isopropyl alcohol 357.6 mg/mL	26.8	22.1	23.0	11.6
isopropyl alcohol 715.3 mg/mL	8.5	8.3	10.2	8.7
alanine 50 mg/mL	48.2	36.9	36.3	37.3
alanine 100 mg/mL	43.9	36.6	34.0	38.0
alanine 150 mg/mL	36.8	36.0	31.8	38.1
ubiquitin 10 mg/mL	50.2	37.2	36.4	38.0
ubiquitin 20 mg/mL	49.8	36.7	35.9	39.1

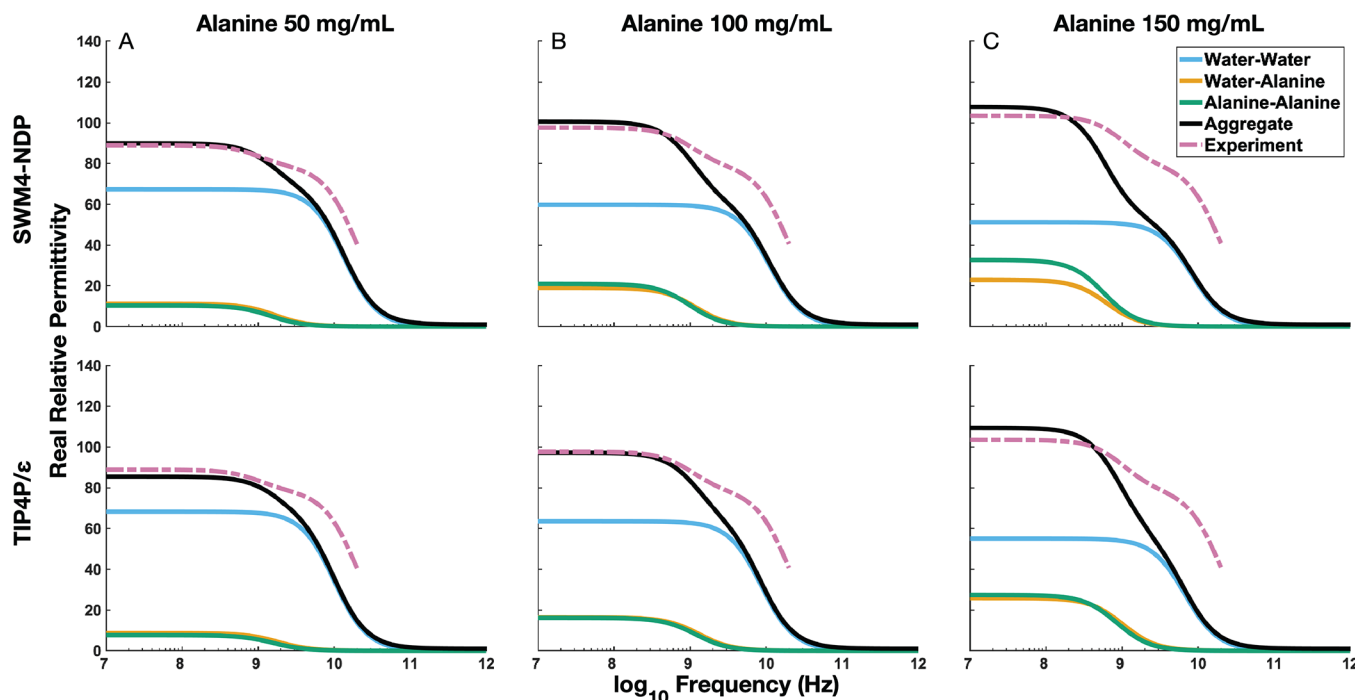


**Figure 3.** Real part of the complex permittivity for alanine solutions at three different concentrations: (A) 50, (B) 100, and (C) 150 mg/mL. Two water models (TIP4P/ $\epsilon$  and SWM4-NDP) were used for simulations (red curves) and compared to the experimentally determined permittivity (green broken curves). The simulated permittivity is further broken down into contributions from different interactions (blue, orange, and green solid lines). The imaginary component from the same simulations is in Figure S8, and the second replicas are found in Figure S9.

which is attached to the oxygen atom via a zero-length harmonic spring and captures part of the polarizability of water molecules. This results in the increased accuracy of the permittivity but at the expense of requiring more computational resources (roughly a factor of 4 $\times$  simulation time).

**IPA Solution Permittivity.** After comparing permittivity for pure water between simulations and experiments, we next considered solutions of isopropyl alcohol (IPA). The relative permittivity of IPA alone is  $\sim$ 20 at 300 K,<sup>20</sup> which is much lower than that of water. Therefore, as the concentration of IPA increases, the relative real permittivity decreases, as can be seen in both our measured and modeled results, taken at concentrations of 715.3, 357.6, 178.8, and 89.4 mg/mL (Figure S5). Additionally, the resonance peak for IPA occurs at a lower frequency than that of water. As the concentration of IPA increases, more IPA and more interactions between IPA and water shift the system resonances to lower frequencies (Figure S6). Our simulation and measurement data agree well with Sato et al.<sup>20</sup> Simulation repetitions are shown in Figure S7.

All tested water models consistently overestimate both the frequency and magnitude of the peak imaginary permittivity for IPA dilutions. The TIP3P water model has the largest discrepancy, while the TIP4P/ $\epsilon$  and SWM4-NDP models perform better. Both TIP4P/ $\epsilon$  and SWM4-NDP fail to capture the steep dropoff in peak magnitude as the concentration of IPA is increased. The modeled permittivity from both water models approaches the correct peak magnitude at the highest IPA concentration, but both models still predict a higher resonance frequency than experiment.

**Alanine Solution Permittivity.** Next, the dielectric properties of alanine solutions with TIP3P, TIP4P, TIP4P/ $\epsilon$ , and SWM4-NDP water models in simulations were analyzed and compared with both our own experimental data and with published data.<sup>26</sup> A simulation volume of alanine solution is

shown in Figure S10. The static (low-frequency) permittivity of alanine in TIP3P water is larger than the experimental value for the 50 and 100 mg/mL systems, which is consistent with previous observations.<sup>26</sup> In experiments, as the concentration of alanine increases, the permittivity of the system increases (Figure 3). However, in simulations, the system permittivity with the TIP3P water model does not increase when the alanine concentration increases from 100 mg/mL to 150 mg/mL (Figure S11). This discrepancy is likely caused by the abnormally high permittivity of the TIP3P water model on its own (Figure 2A).

For systems using TIP4P/ $\epsilon$  with CHARMM36m (non-polarizable) and SWM4-NDP with Drude-2013 (polarizable) force fields, the simulated permittivity increases when the concentration of alanine increases, which is consistent with experimental results. Additionally, the low-frequency permittivity shows close agreement with our experimental values at all concentrations. The frequencies of the two modeled resonance peaks for alanine solutions at  $\sim$ 1 GHz and  $\sim$ 10 GHz agree closely with our measurements (Figures 3 and S11), although the magnitudes of the modeled resonances are slightly larger than the measured ones.

In addition to the net permittivity, we also separated out the permittivity contribution from each of the system components, i.e., the dipole correlations corresponding to water-water, water-alanine, and alanine-alanine interactions (Figure 3). While the experimental permittivity cannot discern between the different interaction terms, the modeled permittivity can be divided into its constituent interactions. In Figure 3, one can see that the first resonance stems jointly from the water-alanine and alanine-alanine terms, while the second is due to the water self-interaction. The self-resonance of water occurs at a higher frequency than that of alanine. The resonance of pure water is also higher than that of water in solution, indicating that the

solute dampens the water and lengthens its relaxation time. The permittivity contribution due to the water self-interaction is also reduced as the concentration of alanine increases. This is due to alanine molecules replacing water in a box with a fixed volume, so the number of water-water interactions decreases. The permittivity contributions from both the water-alanine cross-term and alanine self-term are increased as the alanine concentration is raised.

The TIP4P/ $\epsilon$  model permittivity is closer to our experimental results than SWM4-NDP across both concentration and frequency. This is primarily because the Drude model predicts the alanine-alanine and water-alanine resonances to be at lower frequencies and higher magnitudes than TIP4P/ $\epsilon$ , leading to a larger peak separation from the water-water peak and a steeper real permittivity dropoff at lower frequencies. However, both TIP4P/ $\epsilon$  and SWM4-NDP models overestimate the magnitude of the alanine-alanine and water-alanine interactions, causing a discrepancy between measured and modeled permittivity curves.

Imaginary relative permittivities of alanine solutions with different concentrations were calculated as well (Figure S8). The imaginary system permittivity with the TIP3P water model exceeds the experimental values at alanine concentrations of 50 and 100 mg/mL (Figure S8A,B), which can be explained by the fact that the TIP3P water model consistently over-represents the permittivity (Figure 2B). Even though decreasing the water concentration decreases the system's permittivity, the shape of the system permittivity with TIP3P water still does not fit the experimental curve in the 150 mg/mL system (Figure S8C) because the magnitudes of the alanine-alanine and water-alanine peaks are overestimated.

The system permittivities with the TIP4P/ $\epsilon$  and SWM4-NDP water models have similar magnitude and shape to the experimental values at low concentration. However, as more alanine molecules were added, deviations from experimental values grew (Figure S8B,C). Both the TIP4P/ $\epsilon$  and the SWM4-NDP systems overestimate the alanine-alanine and water-alanine interaction magnitude as the alanine concentration is increased.

**Ubiquitin Solution Permittivity.** To further approximate realistic biological systems and test the possibility of utilizing MD simulations to calculate the permittivity of large molecules in solution, we built two systems with the protein ubiquitin at two different concentrations: 10 and 20 mg/mL. Because of the size of ubiquitin, these systems contained only a single copy in an appropriately sized water box (Figure 4) and were run for 250 ns.

Our modeled permittivity curves match closely with our experiments as well as prior experiments in the literature.<sup>28</sup> The ubiquitin resonances (Figures 5 and S12) can be easily distinguished from the resonances for alanine (Figures 3 and S11), which are at higher frequencies near 10<sup>9</sup> Hz. Compared to the resonance of pure water (Figure 2B), the water self-interaction resonance in ubiquitin solutions only shifts slightly when ubiquitin is added (Table 1). The resonance frequency shift between pure water systems and ubiquitin solutions is small because of the low concentration and the low surface area to volume ratio of ubiquitin, both of which lead to less interactions between solvent and solute.

As the experimental setup only covered a frequency range from 10 MHz to 20 GHz, only half of the ubiquitin resonance was captured in the frequency-domain output from the network analyzer. The experimental permittivity data were

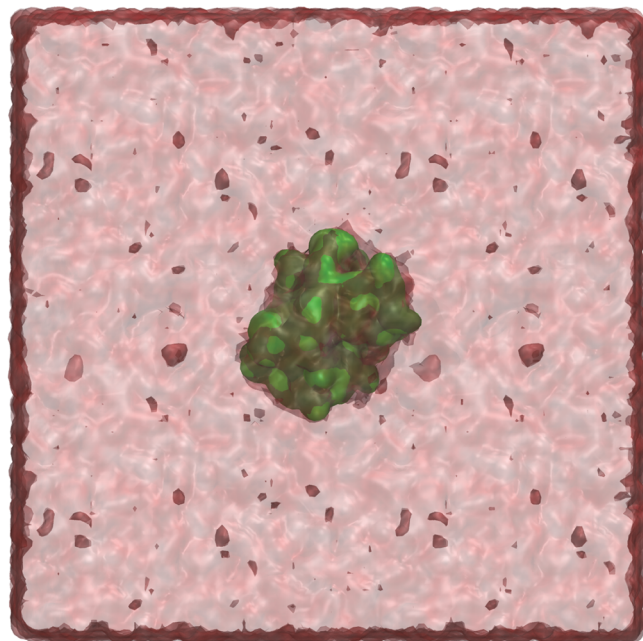


**Figure 4.** Simulation volume with a single copy of ubiquitin in water at an effective concentration of 10 mg/mL.

generated by a Levenberg–Marquardt approximation of the Debye resonances, so the resulting experimental curve was best-fit to values that only fully included the water-water resonance. Both sides of the resonance in the frequency domain are needed to resolve the feature in the time domain, so our experimental curves do not fully capture the low-frequency resonances of ubiquitin solutions. Nonetheless, our experimental imaginary permittivity over frequency agrees well with our simulations (Figure S13) and prior experiments.<sup>28</sup>

## CONCLUSION

In this paper, we determined the microwave dielectric permittivity of aqueous solutions using MD simulations and open-ended coaxial probe measurements. From simulations, the solution permittivity was computed through nonlinear fitting of the dipole auto/cross-correlation functions. Experimentally, a coaxial probe was inserted into each solution to measure the complex reflection coefficient, which was then compared to known solutions to calibrate and compute the permittivity of the unknown solution.

We compared the measured and modeled permittivity of pure water as well as solutions of isopropyl alcohol, alanine, and ubiquitin using multiple simulation force fields. We found that simulations of a pure water box using the TIP3P and TIP4P water models over- and underestimated, respectively, the real permittivity in the low-frequency limit. In contrast, both the TIP4P/ $\epsilon$  and SWM4-NDP water models were more accurate (Figure 2). A similar pattern was observed for solutions of IPA, alanine, and ubiquitin, for which the modeled low-frequency permittivities and resonances were closer to experimental values when using TIP4P/ $\epsilon$  + CHARMM36m or SWM4-NDP + Drude-2013 force fields (Figures 3, 5, and S5).

The dielectric-tuned TIP4P water model (TIP4P/ $\epsilon$ ) combined with the CHARMM36m force field accurately captured the permittivity of both pure water and solutions. The polarizable force fields (SWM4-NDP and Drude-2013) also captured the permittivity in the modeled systems without

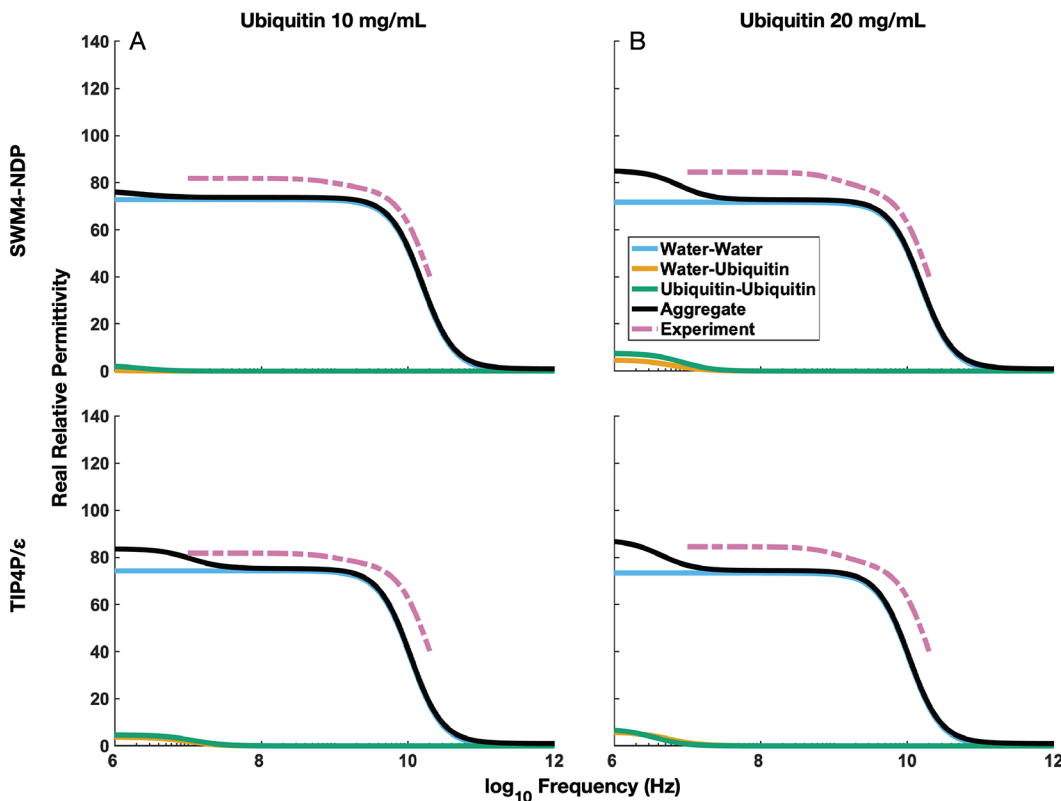


**Figure 5.** Simulated (red solid line) and measured (green broken line) real permittivity for solutions of ubiquitin in water at (A) 10 mg/mL and (B) 20 mg/mL. The simulated permittivity is further broken down into contributions from different interactions (blue, orange, and green solid lines). The imaginary component from the same simulations is in Figure S13, and the second replicas are found in Figure S14.

dielectric-specific tuning. Although the polarizable model carries a notable ( $4\times$ ) increase in computational burden, it more accurately represents the underlying dielectric permittivity phenomena, which may be required to model complex solutions. However, the TIP4P/ $\epsilon$  water model accompanied by the CHARMM36m protein force field may be acceptable for many applications at a reduced computational cost. Further investigation will be needed to ascertain force field suitability for modeling increasingly complex bionanotechnological devices.

## ASSOCIATED CONTENT

### Supporting Information

The Supporting Information is available free of charge at <https://pubs.acs.org/doi/10.1021/acs.jpcb.2c05260>.

Analysis of additional replicas, IPA permittivity curves, and imaginary component of permittivity for all solution systems ([PDF](#))

## AUTHOR INFORMATION

### Corresponding Author

James C. Gumbart — School of Physics, Georgia Institute of Technology, Atlanta, Georgia 30332, United States;  
[ORCID iD](https://orcid.org/0000-0002-1510-7842); Email: [gumbart@physics.gatech.edu](mailto:gumbart@physics.gatech.edu)

### Authors

Alex Saad-Falcon — Georgia Tech Research Institute, Atlanta, Georgia 30332, United States  
 Zijian Zhang — School of Physics, Georgia Institute of Technology, Atlanta, Georgia 30332, United States

David Ryoo — Interdisciplinary Bioengineering Graduate Program, Georgia Institute of Technology, Atlanta, Georgia 30332, United States

James Dee — Georgia Tech Research Institute, Atlanta, Georgia 30332, United States

Ryan S. Westafer — Georgia Tech Research Institute, Atlanta, Georgia 30332, United States

Complete contact information is available at:  
<https://pubs.acs.org/10.1021/acs.jpcb.2c05260>

### Author Contributions

A.S.-F. and Z.Z. contributed equally to this work.

### Notes

The authors declare no competing financial interest.

## ACKNOWLEDGMENTS

This work was supported by Georgia Tech Research Institute (GTRI) Independent Research and Development (IR&D) funds and hosted by Doug Denison in the Advanced Concepts Laboratory. Computational resources were provided through the Extreme Science and Engineering Discovery Environment (XSEDE; TG-MCB130173), which is supported by the National Science Foundation (NSF; ACI-1548562). This work also used the Hive cluster, which is supported by the NSF (1828187) and managed by the Partnership for an Advanced Computing Environment (PACE) at GT. We would also like to thank the following GTRI researchers: Charlie Hunter for help with the RF experimental setup; Tabitha Rosenbalm and True Merrill for sample preparation; David Reid for measurement postprocessing discussion; and Bobby Blake and Amanda Kieffer for help with graphics.

## ■ REFERENCES

- (1) MacMillen, D.; Camposano, R.; Hill, D.; Williams, T. An Industrial View of Electronic Design Automation. *IEEE Trans. Comput.-Aided Des. Integr. Circuits Syst.* **2000**, *19*, 1428–1448.
- (2) Khoshbin, Z.; Housaindokht, M. R.; Izadyar, M.; Bozorgmehr, M. R.; Verdian, A. Recent Advances in Computational Methods for Biosensor Design. *Biochim. Biophys. Acta* **2021**, *118*, 555–578.
- (3) Wells, D. B.; Belkin, M.; Comer, J.; Aksimentiev, A. Assessing Graphene Nanopores for Sequencing DNA. *Nano Lett.* **2012**, *12*, 4117–4123.
- (4) Alfaro, J. A.; Bohländer, P.; Dai, M.; Filius, M.; Howard, C. J.; van Kooten, X. F.; Ohayon, S.; Pomorski, A.; Schmid, S.; Aksimentiev, A.; et al. The Emerging Landscape of Single-Molecule Protein Sequencing Technologies. *Nat. Methods* **2021**, *18*, 604–617.
- (5) Casalini, T.; Limongelli, V.; Schmutz, M.; Som, C.; Jordan, O.; Wick, P.; Borchard, G.; Perale, G. Molecular Modeling for Nanomaterial-Biology Interactions: Opportunities, Challenges, and Perspectives. *Front. Bioeng. Biotechnol.* **2019**, *7*, 268.
- (6) Hemmig, E. A.; Fitzgerald, C.; Maffeo, C.; Hecker, L.; Ochmann, S. E.; Aksimentiev, A.; Tinnefeld, P.; Keyser, U. F. Optical Voltage Sensing Using DNA Origami. *Nano Lett.* **2018**, *18*, 1962–1971.
- (7) Ochmann, S. E.; Joshi, H.; Büber, E.; Franquelim, H. G.; Stegemann, P.; Saccà, B.; Keyser, U. F.; Aksimentiev, A.; Tinnefeld, P. DNA Origami Voltage Sensors for Transmembrane Potentials with Single-Molecule Sensitivity. *Nano Lett.* **2021**, *21*, 8634–8641.
- (8) Mehrotra, P.; Chatterjee, B.; Sen, S. EM-Wave Biosensors: A Review of RF, Microwave, mm-Wave and Optical Sensing. *Sensors* **2019**, *19*, 1013.
- (9) Kirkwood, J. G. The Dielectric Polarization of Polar Liquids. *J. Chem. Phys.* **1939**, *7*, 911–919.
- (10) Cole, R. H. Correlation Function Theory of Dielectric Relaxation. *J. Chem. Phys.* **1965**, *42*, 637–643.
- (11) Fatuzzo, E.; Mason, P. R. A Theory of Dielectric Relaxation in Polar Liquids. *Proc. Phys. Soc.* **1967**, *90*, 741–750.
- (12) Klug, D. D.; Kranbuehl, D. E.; Vaughan, W. E. Molecular Correlation Functions and Dielectric Relaxation. *J. Chem. Phys.* **1969**, *50*, 3904–3905.
- (13) Nee, T.-W.; Zwanzig, R. Theory of Dielectric Relaxation in Polar Liquids. *J. Chem. Phys.* **1970**, *52*, 6353–6363.
- (14) de Leeuw, S. W.; Perram, J. W.; Smith, E. R. Simulation of Electrostatic Systems in Periodic Boundary Conditions. I. Lattice Sums and Dielectric Constants. *Proc. R. Soc. London A. Math. Phys. Sci.* **1980**, *373*, 27–56.
- (15) Neumann, M.; Steinhauser, O. On the Calculation of the Frequency-Dependent Dielectric Constant in Computer Simulations. *Chem. Phys. Lett.* **1983**, *102*, 508–513.
- (16) Boresch, S.; Höchtl, P.; Steinhauser, O. Studying the Dielectric Properties of a Protein Solution by Computer Simulation. *J. Phys. Chem. B* **2000**, *104*, 8743–8752.
- (17) Heinz, T. N.; van Gunsteren, W. F.; Hünenberger, P. H. Comparison of Four Methods to Compute the Dielectric Permittivity of Liquids from Molecular Dynamics Simulations. *J. Chem. Phys.* **2001**, *115*, 1125.
- (18) Marsland, T.; Evans, S. Dielectric Measurements with an Open-Ended Coaxial Probe. *IEE Proc.* **1987**, *134*, 341–349.
- (19) Kaatze, U. Complex Permittivity of Water as a Function of Frequency and Temperature. *J. Chem. Eng. Data* **1989**, *34*, 371–374.
- (20) Sato, T.; Chiba, A.; Nozaki, R. Composition-Dependent Dynamical Structures of 1-Propanol Water Mixtures Determined by Dynamical Dielectric Properties. *J. Chem. Phys.* **2000**, *113*, 9748–9758.
- (21) Jorgensen, W. L.; Chandrasekhar, J.; Madura, J. D.; Impey, R. W.; Klein, M. L. Comparison of Simple Potential Functions for Simulating Liquid Water. *J. Chem. Phys.* **1983**, *79*, 926–935.
- (22) Fuentes-Azcatl, R.; Alejandre, J. Non-polarizable Force Field of Water Based on the Dielectric Constant: TIP4P/ $\epsilon$ . *J. Phys. Chem. B* **2014**, *118*, 1263–1272.
- (23) Huang, J.; Rauscher, S.; Nawrocki, G.; Ran, T.; Feig, M.; de Groot, B. L.; Grubmüller, H.; MacKerell, A. D. CHARMM36m: An Improved Force Field for Folded and Intrinsically Disordered Proteins. *Nat. Methods* **2017**, *14*, 71–73.
- (24) Lamoureux, G.; Harder, E.; Vorobyov, I. V.; Roux, B.; MacKerell, A. D., Jr. A Polarizable Model of Water for Molecular Dynamics Simulations of Biomolecules. *Chem. Phys. Lett.* **2006**, *418*, 245–249.
- (25) Lopes, P. E.; Huang, J.; Shim, J.; Luo, Y.; Li, H.; Roux, B.; MacKerell, A. D. Force Field for Peptides and Proteins Based on the Classical Drude Oscillator. *J. Chem. Theory Comput.* **2013**, *9*, 5430–5449.
- (26) Cifra, M.; Průša, J.; Havelka, D.; Krivosudský, O. Water Models in Molecular Dynamics Simulation Prediction of Dielectric Properties of Biomaterials. *IEEE J. Electromagn. RF Microw. Med. Biol.* **2019**, *3*, 97–104.
- (27) Vijay-Kumar, S.; Bugg, C. E.; Cook, W. J. Structure of Ubiquitin Refined at 1.8 Å Resolution. *J. Mol. Biol.* **1987**, *194*, 531–544.
- (28) Knocke, A.; Weingärtner, H. The Dielectric Spectrum of Ubiquitin in Aqueous Solution. *J. Phys. Chem. B* **2001**, *105*, 3635–3638.
- (29) Phillips, J. C.; Braun, R.; Wang, W.; Gumbart, J.; Tajkhorshid, E.; Villa, E.; Chipot, C.; Skeel, R. D.; Kalé, L.; Schulten, K. Scalable Molecular Dynamics with NAMD. *J. Comput. Chem.* **2005**, *26*, 1781–1802.
- (30) Phillips, J. C.; Hardy, D. J.; Maia, J. D. C.; Stone, J. E.; Ribeiro, J. V.; Bernardi, R. C.; Buch, R.; Fiorin, G.; Hénin, J.; Jiang, W.; et al. Scalable Molecular Dynamics on CPU and GPU Architectures with NAMD. *J. Chem. Phys.* **2020**, *153*, 044130.
- (31) Lamoureux, G.; Roux, B. Modeling Induced Polarization with Classical Drude Oscillators: Theory and Molecular Dynamics Simulation Algorithm. *J. Chem. Phys.* **2003**, *119*, 3025–3039.
- (32) Jiang, W.; Hardy, D. J.; Phillips, J. C.; MacKerell, A. D., Jr.; Schulten, K.; Roux, B. High-Performance Scalable Molecular Dynamics Simulations of a Polarizable Force Field Based on Classical Drude Oscillators in NAMD. *J. Phys. Chem. Lett.* **2011**, *2*, 87–92.
- (33) Darden, T. A.; York, D. M.; Pedersen, L. G. Particle mesh Ewald: An  $N\log(N)$  Method for Ewald Sums in Large Systems. *J. Chem. Phys.* **1993**, *98*, 10089–10092.
- (34) Greengard, L.; Rokhlin, V. A Fast Algorithm for Particle Simulations. *J. Comput. Phys.* **1987**, *73*, 325–348.
- (35) van der Spoel, D.; van Maaren, P. J.; Berendsen, H. J. C. A Systematic Study of Water Models for Molecular Simulation: Derivation of Water Models Optimized for Use with a Reaction Field. *J. Chem. Phys.* **1998**, *108*, 10220–10230.
- (36) Humphrey, W.; Dalke, A.; Schulten, K. VMD: Visual Molecular Dynamics. *J. Mol. Graphics* **1996**, *14*, 33–38.
- (37) Smith, P. E.; Brame, R. M.; Mark, A. E.; van Gunsteren, W. F. Dielectric Properties of Trypsin Inhibitor and Lysozyme Calculated from Molecular Dynamics Simulations. *J. Phys. Chem.* **1993**, *97*, 2009–2014.
- (38) Berne, B. J.; Harp, G. D. *Advances in Chemical Physics*; John Wiley & Sons, Ltd.: 1970; pp 63–227, DOI: [10.1002/9780470143636.ch3](https://doi.org/10.1002/9780470143636.ch3).
- (39) Kelley, C. T. *Iterative Methods for Optimization*; Society for Industrial and Applied Mathematics: 1999, DOI: [10.1137/1.9781611970920](https://doi.org/10.1137/1.9781611970920).
- (40) Madsen, K.; Nielsen, H. B.; Tingleff, O. *Methods for Non-Linear Least Squares Problems*, 2nd ed.; 2004.
- (41) Caillol, J. M.; Levesque, D.; Weis, J. J. Theoretical Calculation of Ionic Solution Properties. *J. Chem. Phys.* **1986**, *85*, 6645–6657.
- (42) Caillol, J. M.; Levesque, D.; Weis, J. J. Electrical Properties of Polarizable Ionic Solutions. I. Theoretical Aspects. *J. Chem. Phys.* **1989**, *91*, 5544–5554.
- (43) Caillol, J. M.; Levesque, D.; Weis, J. J. Electrical Properties of Polarizable Ionic Solutions. II. Computer Simulation Results. *J. Chem. Phys.* **1989**, *91*, 5555–5566.
- (44) Xu, D.; Phillips, J. C.; Schulten, K. Protein Response to External Electric Fields: Relaxation, Hysteresis, and Echo. *J. Phys. Chem.* **1996**, *100*, 12108–12121.

- (45) Yoon, T. J.; Maerzke, K. A.; Currier, R. P.; Findikoglu, A. T. PyOCP: A Flexible Open-Source Software Library for Estimating and Modeling the Complex Permittivity Based on the Open-Ended Coaxial Probe (OECP) Technique. 2021, arXiv:2109.14889. *arXiv [physics]*. <https://arxiv.org/abs/2109.14889> (accessed 2022-03-10).
- (46) Gregory, A. P.; Clarke, R. N. *Tables of the Complex Permittivity of Dielectric Reference Liquids at Frequencies up to 5 GHz*; NPL Report; 2012.
- (47) Barthel, J.; Bachhuber, K.; Buchner, R.; Hetzenauer, H. Dielectric Spectra of Some Common Solvents in the Microwave Region. Water and Lower Alcohols. *Chem. Phys. Lett.* **1990**, *165*, 369–373.

## □ Recommended by ACS

### Impact of the Force Field on the Calculation of Density and Surface Tension of Epoxy–Resins

Mathilde Orselly, Patrice Malfreyt, *et al.*

MARCH 14, 2023

THE JOURNAL OF PHYSICAL CHEMISTRY B

READ 

### Effect of Ammonium Sulfate on the Solubility of $\alpha$ -Form and $\beta$ -Form L-Glutamic Acid in Water and Actual Fermentation Mother Liquor from 278.15 to 333.15 K

Rui Wang, Wei Cong, *et al.*

FEBRUARY 16, 2023

INDUSTRIAL & ENGINEERING CHEMISTRY RESEARCH

READ 

### Application of the Gaussian Process Regression Method Based on a Combined Kernel Function in Engine Performance Prediction

Xiuyong Shi, Yunfang Liang, *et al.*

NOVEMBER 03, 2022

ACS OMEGA

READ 

### Wall Effects for Spheroidal Particle in Confined Bingham Plastic Fluids

Juan Dang, Shuai Tian, *et al.*

OCTOBER 21, 2022

ACS OMEGA

READ 

[Get More Suggestions >](#)